UCLA
UCLA Previously Published Works

Title
Development of a land surface model with coupled snow and frozen soil physics

Authors
Wang, Lei
Zhou, Jing
Qi, Jia
et al.
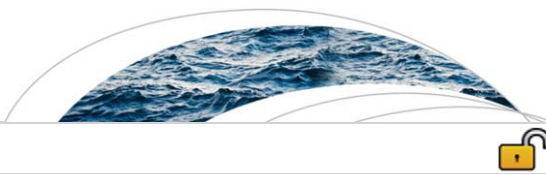
RESEARCH ARTICLE

Key Points:
- A new LSM with coupled snow and frozen soil physics was developed
- Enthalpy was adopted as a prognostic variable instead of snow/soil temperature
- The LSM simulated upward moisture fluxes toward the freezing front

Supporting Information:
- Supporting Information S1
- Figure S1
- Figure S2
- Figure S3
- Figure S4
- Figure S5

Correspondence to:
L. Wang,
wanglei@itpcas.ac.cn;
J. Zhou,
zhoujing@itpcas.ac.cn

Development of a land surface model with coupled snow and frozen soil physics

Lei Wang[1,2,3] [ID], Jing Zhou[1] [ID], Jia Qi[1,3] [ID], Litao Sun[1,3], Kun Yang[1,2,3] [ID], Lide Tian[1,2,3] [ID], Yanluan Lin[4], Wenbin Liu[5] [ID], Maheswor Shrestha[6] [ID], Yongkang Xue[7] [ID], Toshio Koike[8], Yaoming Ma[1,2,3], Xiuping Li[1] [ID], Yingying Chen[1,2] [ID], Deliang Chen[9] [ID], Shilong Piao[10] [ID], and Hui Lu[4] [ID]

[1]Key Laboratory of Tibetan Environment Changes and Land Surface Processes, Institute of Tibetan Plateau Research, Chinese Academy of Sciences, Beijing, China, [2]CAS Center for Excellence in Tibetan Plateau Earth Sciences, Beijing, China, [3]University of Chinese Academy of Sciences, Beijing, China, [4]Department of Earth System Science, Tsinghua University and Key Laboratory of Numerical Simulation for Earth System, Ministry of Education, Beijing, China, [5]Institute of Geographic Sciences and Natural Resources Research, Chinese Academy of Sciences, Beijing, China, [6]Water and Energy Commission Secretariat, Kathmandu, Nepal, [7]Department of Geography, University of California, Los Angeles, Los Angeles, California, USA, [8]Department of Civil Engineering, University of Tokyo, Tokyo, Japan, [9]Department of Earth Sciences, University of Gothenburg, Gothenburg, Sweden, [10]Sino-French Institute for Earth System Science, College of Urban and Environmental Sciences, Peking University, Beijing, China

Abstract Snow and frozen soil are important factors that influence terrestrial water and energy balances through snowpack accumulation and melt and soil freeze-thaw. In this study, a new land surface model (LSM) with coupled snow and frozen soil physics was developed based on a hydrologically improved LSM (HydroSiB2). First, an energy-balance-based three-layer snow model was incorporated into HydroSiB2 (hereafter HydroSiB2-S) to provide an improved description of the internal processes of the snow pack. Second, a universal and simplified soil model was coupled with HydroSiB2-S to depict soil water freezing and thawing (hereafter HydroSiB2-SF). In order to avoid the instability caused by the uncertainty in estimating water phase changes, enthalpy was adopted as a prognostic variable instead of snow/soil temperature in the energy balance equation of the snow/frozen soil module. The newly developed models were then carefully evaluated at two typical sites of the Tibetan Plateau (TP) (one snow covered and the other snow free, both with underlying frozen soil). At the snow-covered site in northeastern TP (DY), HydroSiB2-SF demonstrated significant improvements over HydroSiB2-F (same as HydroSiB2-SF but using the original single-layer snow module of HydroSiB2), showing the importance of snow internal processes in three-layer snow parameterization. At the snow-free site in southwestern TP (Ngari), HydroSiB2-SF reasonably simulated soil water phase changes while HydroSiB2-S did not, indicating the crucial role of frozen soil parameterization in depicting the soil thermal and water dynamics. Finally, HydroSiB2-SF proved to be capable of simulating upward moisture fluxes toward the freezing front from the underlying soil layers in winter.

1. Introduction

Snow and frozen soil are components of the cryosphere that require careful treatment in land surface hydrological modeling due to their wide distributions around the world [*Essery et al.*, 2009]. Both snow and frozen soil influence the storage and transmission of water in cold regions [*Woo*, 2012] where climate warming is expected to be most severe.

Snow with its high albedo, low roughness and relatively low thermal conductivity, can not only store and release water within the water cycles but also have a significant influence on land-atmosphere interactions [see *Essery et al.*, 1999; *Zhang*, 2005; *Shrestha et al.*, 2012]. Pore ice in frozen soil reduces its infiltration capacity, leading to a higher proportion of snowmelt and spring rainfall being partitioned into surface runoff [*Stähli et al.*, 1999]. Moreover, the phase transitions between the ice and liquid water alter the energy distribution in the soil and have an important influence on the upper snow layer [see *Niu and Yang*, 2006]. In winter, the frozen soil occupies 55–60% of the land surface in the Northern Hemisphere [*Zhang et al.*, 1999] and 72% of the Chinese territory [*Li et al.*, 2008]. The reduction or expansion of permafrost, mainly contained in

the high-latitude or high-altitude regions, is a key response to climate change at long time scales [*Kurylyk et al.*, 2014; *Bao et al.*, 2016]. Permafrost thaw induced by rising subsurface temperatures will likely alter surface and subsurface hydrology in high-altitude and/or latitude regions [*Kurylyk et al.*, 2014]. Therefore, snow and frozen soil investigations are critical for both integrated water resource management and climate change adaptation in cold regions at high elevation [*Shrestha et al.*, 2010; *Bao et al.*, 2016]. The snow and frozen soil schemes within a land surface hydrological modeling system should be explicitly addressed.

At present, a few land surface models (LSMs) have parameterized both snow and frozen soil processes [e.g., *Flerchinger and Saxton*, 1989; *Gusev and Nasonova*, 1998; *Koren et al.*, 1999; *Pauwels and Wood*, 1999; *Smirnova et al.*, 2000; *Jansson and Moon*, 2001; *Warrach et al.*, 2001; *Cherkauer et al.*, 2003; *Niu et al.*, 2011; *Xiao et al.*, 2013; *Lebedeva et al.*, 2014]. However, most of the above LSMs utilize temperature as the prognostic variable and then use a threshold freezing point to determine the phase change of water. This process has inevitably produced instability issues with mass or heat conservation during numerical simulations [*Hansson et al.*, 2004]. When water phase change occurs across a freezing point, a sudden variation in the bulk (soil and water) hydraulic and thermal properties, especially a dramatic change in soil hydraulic conductivity, will occur, and this results in numerical instability issues when solving the coupled energy and water balance equations. In recent years, in order to avoid the instability caused by the uncertainty in estimating water phase changes, enthalpy has been adopted as a prognostic variable in the calculation of snow accumulation and melting [*Sun and Xue*, 2001] and in the simulation of soil heat and water transport [*Q. Li et al.*, 2009; *Dall'Amico et al.*, 2011] in energy balance equations. However, until now, a robust LSM that uses enthalpy to consistently calculate coupled snow and frozen soil schemes has not been developed.

The objective of this study is to develop a simple cryosphere LSM with coupled snow and frozen soil schemes from the perspective of enthalpy. A second objective is to carefully evaluate the newly developed LSM by using yearlong observations from two representative stations (one snow free and one seasonally snow covered) in the Tibetan Plateau (TP). The paper is organized as follows. Section 2 describes the model development. The study region and data sets are introduced in section 3. Section 4 presents the model evaluations and applications at two sites of the TP. Conclusions are presented in section 5.

2. Model Development

2.1. Model Structure

The base model used in this study is the hydrologically improved LSM [*Wang et al.*, 2009a], which consists of an improved hydrological description of the simple biosphere model 2 (SiB2) [*Sellers et al.*, 1996] (so-called HydroSiB2) based on three aspects. First, the SiB2 three-layer soil model is replaced with a multilayer soil column coupled to a lumped unconfined aquifer model. Next, lateral water flows are described in the updated soil model. Finally, the soil hydraulic function in SiB2 is replaced with van Genuchten parameterization [*van Genuchten*, 1980], and exponential vertical soil heterogeneity is described. Given the above improvements compared to most one-dimensional LSMs (e.g., SiB2), HydroSiB2 was selected for developing the cryosphere land surface modeling in this study.

The main steps of the model development in this study are as follows. First, the three-layer energy balance snow module from the Water and Energy Budget based Distributed Hydrological Model (WEB-DHM) [*Wang et al.*, 2009b, 2009c; *Jaranilla-Sanchez et al.*, 2011; *Wang et al.*, 2012; *Qi et al.*, 2015; *Zhou et al.*, 2015] with improved snow physics (so-called WEB-DHM-S) [*Shrestha et al.*, 2010, 2012, 2014] was fully coupled with the HydroSiB2. The snow module has combined the intermediate complexity snow parameterization from the Simplified Simple Biosphere Model Version 3 [*Sun et al.*, 1999; *Sun and Xue*, 2001; *Xue et al.*, 1991, 2003] and the albedo scheme from the Biosphere-Atmosphere Transfer Scheme [*Dickinson et al.*, 1993; *Yang et al.*, 1997]. The HydroSiB2 model with the newly coupled snow module is called HydroSiB2-S hereinafter. Second, a new frozen soil scheme developed by *Li and Sun* [2008], which modifies the governing equations by considering the liquid and solid water phase changes based on enthalpy theory, was incorporated into HydroSiB2-S (hereafter HydroSiB2-SF). The overall model structure of HydroSiB2-SF is shown in Figure 1. The left part of Figure 1 is a schema of the energy balance process for HydroSiB2-SF, while the right part is a diagram indicating the water balance process of HydroSiB2-SF. The base model (HydroSiB2) was used to compute water and energy fluxes between the lower atmosphere and land surface. Then, vertical water distributions (surface storage, subsurface storage, soil moisture, and groundwater profile) and energy
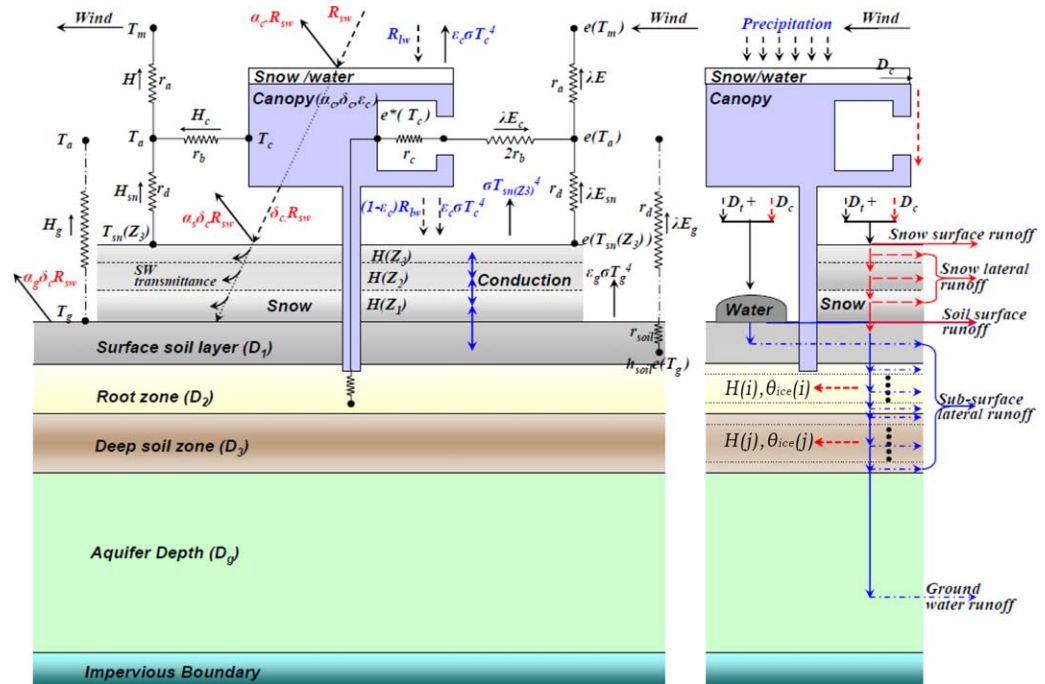
Figure 1. Structure of the new land surface model (HydroSiB2-SF), which has a three-layer snow module coupled with a frozen soil module. T is temperature, $e(T)$ is vapor pressure at T, R_{sw} and R_{lw} are downward shortwave and longwave radiation, H and λE are sensible and latent heats, and ε, δ, and α are emissivity, transmittance, and reflectance, respectively. $H(i)$ and $H(j)$ in the right part are the soil enthalpy used in the frozen soil module, while $\theta_{ice}(i)$ and $\theta_{ice}(j)$ represent the soil ice content in the frozen soil module. Subscript c refers to canopy, g to soil surface, sn to snow surface, and m to the reference height. The figure was modified from *Shrestha et al.* [2010].

distribution (surface and subsurface temperature and sensible and latent heat fluxes) were updated by HydroSiB2-SF. Details of the three-layer energy balance snow module and frozen soil module are described in the following subsections. Definitions of models are given in Table 1, and different model acronyms represent the base model coupled with different snow/frozen soil modules.

2.2. Snow Parameterization

The snow processes were simulated considering two different snow cover conditions. If the snow depth on the canopy/ground was less than 5 cm, the original single-layer snow scheme [*Sellers et al.*, 1996] was adopted; otherwise, the new three-layer snow scheme [*Shrestha et al.*, 2010] was used.

In the three-layer snow scheme, the mass budget for each layer was calculated considering the precipitation, evaporation/condensation, compaction, liquid water retention, snowmelt runoff, and infiltration into the underlying layers. The meltwater in each layer increases with snowmelt and flows into the underlying layer when it exceeds the liquid water-holding capacity. A surface energy balance equation was formulated for only the top layer (the thickness was maintained at a fixed depth of 2 cm), while the heat budget of the second (the maximum thickness was maintained at 20 cm) and third (the remaining body of the snowpack) layers was controlled by heat conduction and penetrating shortwave radiation [*Shrestha et al.*, 2010]. These three layers evolved differently through their own energy budgets and the heat exchanges between them.

Improved from the original snow scheme (bulk snow pack), the new snow module considers the attenuation of shortwave radiation penetrated in a three-layer snow pack. The energy content of the snowpack is

Table 1. Definition of the Models Used in the Study

No.	Model	Description
1	HydroSiB2	Base model with the original single-layer snow module
2	HydroSiB2-F	HydroSiB2 coupled with frozen soil module and using the original single-layer snow module in HydroSiB2
3	HydroSiB2-S	HydroSiB2 with an energy-balance-based three-layer snow model
4	HydroSiB2-SF	HydroSiB2-S coupled with frozen soil module

Table 2. Nomenclature in Snow Parameterization (Section 2.1)

Symbol	Unit	Definition
H	$J\,m^{-3}$	Volumetric enthalpy of water
Z_j	m	Snow depth of layer j
C_v	$J\,m^{-3}\,°C^{-1}$	Mean snow volumetric specific heat capacity
T_{sn}	°C	Snow temperature
f_{ice}		Dry-snow mass fraction of the total mass in the snow layer
h_v	$J\,kg^{-1}$	Latent heat of fusion for ice
ρ_s	$kg\,m^{-3}$	Bulk density of snow
G_{sn}	$W\,m^{-2}$	Heat flux through the snow layer
R_{nsn}	$W\,m^{-2}$	Net radiation
H_{sn}	$W\,m^{-2}$	Sensible heat flux
λE_{sn}	$W\,m^{-2}$	Latent heat flux
G_{pr}	J	Thermal energy from rain at the snow surface
K	$W\,m^{-1}\,°C^{-1}$	Thermal conductivity of snow
K_i	$W\,m^{-1}\,°C^{-1}$	Thermal conductivity of ice, $=2.29$
K_a	$W\,m^{-1}\,°C^{-1}$	Thermal conductivity of air, $=0.023$
SW_{sn}	$W\,m^{-2}$	Shortwave radiation flux absorbed by the snow layer
$M_{snow,j}$	m	Snow water equivalent at snow layer j
P_s	$m\,s^{-1}$	Rate of snowfall
IF_j	$m\,s^{-1}$	$=Min\,(O_j, P_{avs})$, is the actual liquid water infiltration flux at the interface, where O_j is the liquid water outflow rate that will be drained to the underlying layer if the total liquid water in layer exceeds its liquid water-holding capacity, and P_{avs} is the pores available in the layer
R_j	$m\,s^{-1}$	Runoff from the lower interface (of layer j)
E_{sn}	$m\,s^{-1}$	Combined evaporation and sublimation rate

affected by the shortwave radiation penetration, heat conduction between sublayers, ground heat fluxes, the flux of advection due to precipitation, energy due to phase change and net radiation at the surface accompanied by sensible and latent heat fluxes. Specifically, the enthalpy (H) is used as a prognostic variable instead of snow temperature in the energy balance equation, which includes the internal energy of liquid water or ice as well as the energy of the phase change [*Shrestha et al.*, 2010]. The equation for the enthalpy of each snow layer is given as follows (detailed nomenclature and units are listed in Table 2):

$$\frac{\partial H(Z_j)}{\partial_t} = -\frac{\partial G_{sn}(Z_j)}{\partial z} \tag{1}$$

It can be seen that the enthalpy change with time is opposite to the heat flux change with vertical snow depth through each snow layer. H and G_{sn} are defined as

$$H(Z_j) = C_v(Z_j) \times T_{sn}(Z_j) - f_{ice}(Z_j) \times h_v \times \rho_s(Z_j) \tag{2}$$

$$G_{sn}(Z_j) = \begin{cases} R_{nsn} - H_{sn} - \lambda E_{sn} + G_{pr} & \text{at snow surface } (j=3) \\ K(Z_j)\dfrac{\partial[T_{sn}(Z_j) + 273.15]}{\partial z} + SW_{sn}(Z_j) & \text{within snow layers } (j=2,\ 1) \end{cases} \tag{3}$$

From equation (2), enthalpy mainly depends on the heat storage of each snow layer. For the snow surface layer, heat flux is calculated by the energy balance equation. For the second and third layers, heat flux mainly depends on the vertical heat conduction and the absorbed shortwave radiation flux through each snow layer. The thermal conductivity of snow (K) is a function of several variables including the bulk density of snow and the thermal conductivities of ice and air and is calculated as follows [*Shrestha et al.*, 2010]:

$$K = K_a + (7.75 \times 10^{-5}\rho_s + 1.105 \times 10^{-6}\rho_s^2) \times (K_i - K_a) \tag{4}$$

The mass balance for snow is governed by the rate of snowfall, melting, infiltration into the underlying snow layer/soil, evaporation/sublimation, and runoff. The mass balance equations are listed below:

$$\frac{\partial M_{snow,j}}{\partial t} = \begin{cases} P_s + IF_0 - IF_j - R_j - E_{sn} & \text{top layer } (j=3) \\ IF_{j+1} - IF_j - R_j & \text{other layers } (j=2,\ 1) \end{cases} \tag{5}$$

It is assumed that liquid water at its melting point has zero enthalpy so that the phase change processes can be dealt with easily. More detailed descriptions and calculation steps for the three-layer snow module can be found in *Shrestha et al.* [2010].
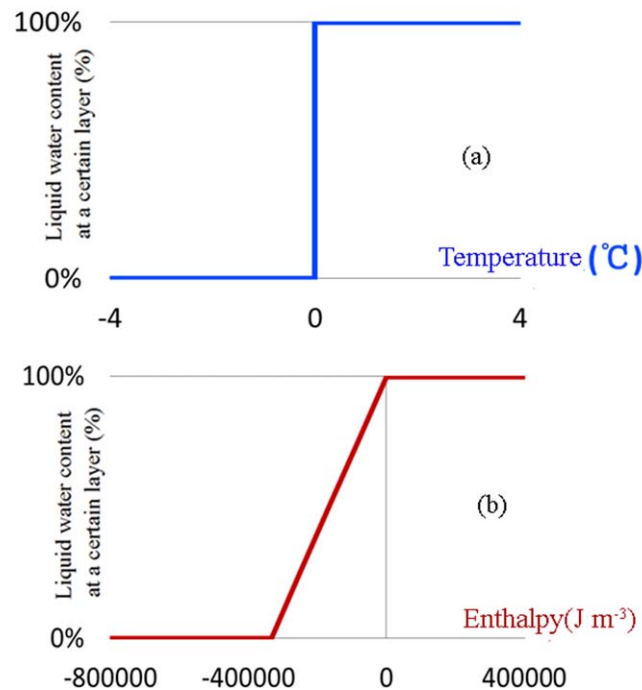
Figure 2. The schematic about the phase transition processes using the (a) temperature and (b) enthalpy as prognostic variables.

2.3. Frozen Soil Parameterization
2.3.1. Frozen Soil Model Description and Computational Steps

The freezing-thawing processes based on the thermodynamic equilibrium state are described by a universal and simplified soil model developed by *Li and Sun* [2008] and *Q. Li et al.* [2009]. This soil model can realistically calculate the coupled water and energy transfer for a variety of soil conditions such as frozen/unfrozen, arid/semiarid conditions. To avoid the difficulty in the calculation of ice-water phase changes, the model utilizes soil enthalpy (H) and total water mass (m_a) for solving the soil temperature and volumetric liquid water content in the respective governing equations. Figure 2 illustrates the liquid-ice phase transition processes, in which the temperature and enthalpy are taken as prognostic variables. For the temperature-based frozen soil model (Figure 2a), the energy in frozen soil layers increases with the liquid fraction increasing from 0 to 100%;

however, since the temperature remains at 0°C, the energy calculation based on temperature will be unstable. In contrast, the enthalpy-index soil model (Figure 2b, for 1 unit mass water) can represent the continuous and gradual variation in energy with the changing liquid fraction, which ensures the stability of the energy calculation. Compared with the discontinuous variations in temperature during freezing/thawing processes, enthalpy can represent both the internal energy and the water phase state, and thereby, the utilization of enthalpy in the model can reflect the continuous and any slight energy variations of the whole soil system during phase transitions [*Bao et al.*, 2016]. Therefore, the soil model developed by *Li and Sun* [2008] was used in this study for frozen soil parameterization.

The main computational steps of the frozen soil model are shown in Figure 3, which will be described in detail below. At each time step, a method proposed by *Ding et al.* [2014] was first used to identify the precipitation types (rain, snow, and sleet) at the two stations. Then, the model enters the frozen soil algorithm, which contains three schemes: heat diffusion scheme, freezing/thawing scheme, and soil moisture movement scheme. The above three schemes can separately solve thermal diffusion, liquid-ice phase change, and water diffusion, but relatively independently and step by step. In the frozen soil algorithm, all available incoming energy first reaches the ground surface, and heat is diffused into the soil column through an energy governing equation. Second, to avoid the instability issues indicated in Figure 2, soil enthalpy and total water mass are used as prognostic variables in the governing equations to replace soil temperature and soil liquid content during the freezing/thawing scheme, which solves the liquid-ice phase change. Simultaneously, the soil temperature, liquid soil moisture, and ice content are calculated. Then, the soil hydraulic properties are modified using the updated soil temperature, liquid water, and ice contents. The vertical soil moisture profile, lateral runoff, overland flow, and groundwater flow are calculated using the updated hydraulic properties. Finally, soil thermal properties estimated from the redistribution of liquid soil moisture and ice are used for the following time step calculation.

2.3.2. Frozen Soil Algorithm

The frozen soil algorithm was adopted from the method of *Li and Sun* [2008] and *Q. Li et al.* [2009], who proposed a new algorithm through variable transformation based on the universal frozen soil parameterization [*Zhao et al.*, 1997]. The universal frozen soil parameterization of coupling heat and water transport mainly has two prognostic equations and three diagnostic equations (see Table 3 for the detailed nomenclature). A
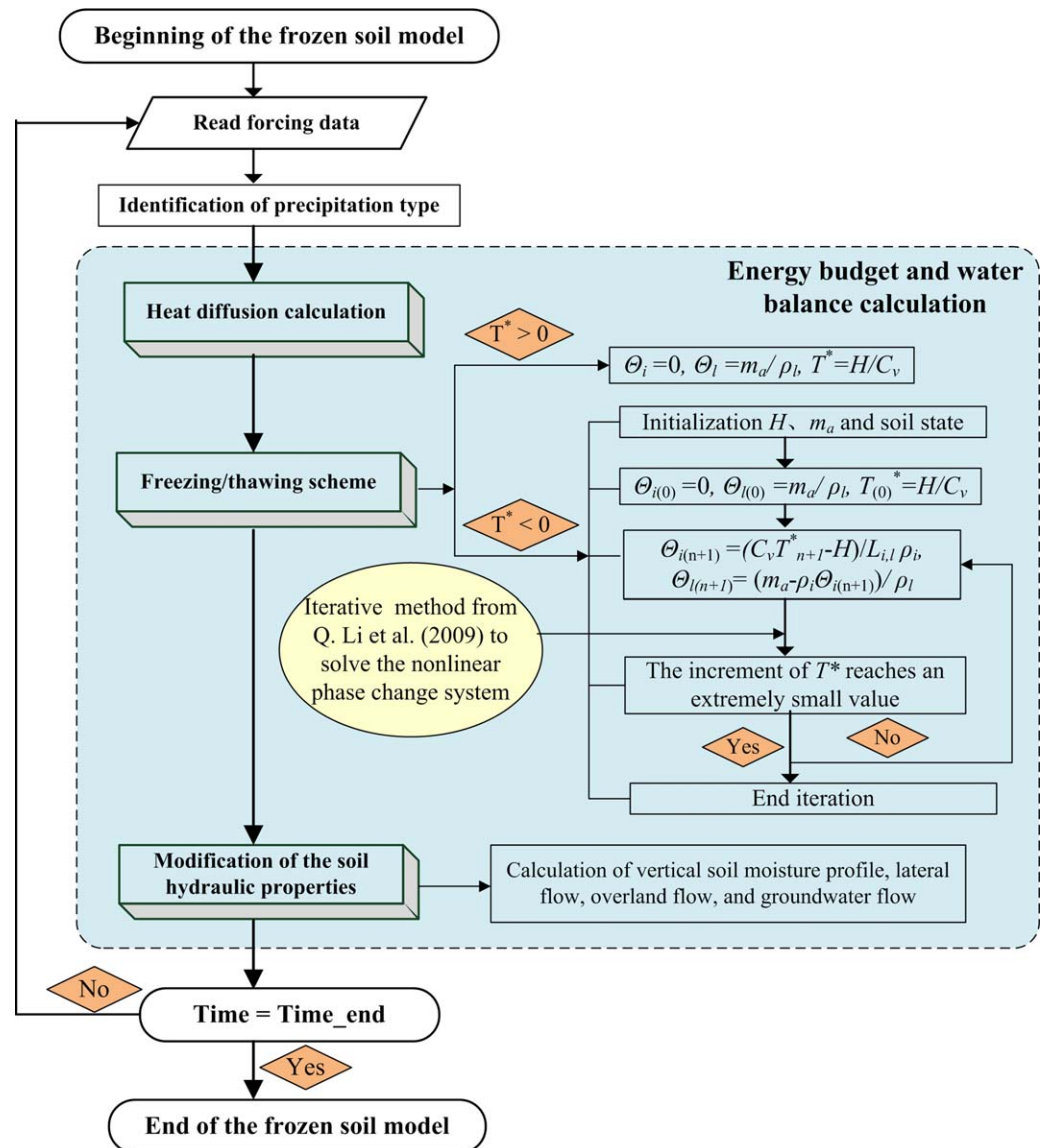
Figure 3. The computational flowchart of the frozen soil model (nomenclature is listed in Table 3).

general energy governing equation for heat flux through the soil column, which also indicates the change in temperature, T^* (°C), is described by the following equation:

$$\frac{\partial C_V T^*}{\partial t} - L_{i,l}\frac{\partial \rho_i \theta_i}{\partial t} = \frac{\partial}{\partial z}\left(K_{eff}\frac{\partial T^*}{\partial z}\right) - \rho_l c_l \frac{\partial u_l T^*}{\partial z} \tag{6}$$

The first term on the left of the equation is the heat storage change with time, while the second term is related to the latent heat due to freezing or thawing. The first term on the right of the equation refers to the vertical conductive heat, while the last term refers to the convective heat that arises from liquid movement.

The change in the volumetric content of water, Q_l, is given by the soil water balance equation as follows:

$$\frac{\partial \theta_l}{\partial t} = -\frac{\rho_i}{\rho_l}\frac{\partial \theta_i}{\partial t} - \frac{\partial}{\partial z}\left(-K_l\frac{\partial \psi}{\partial z} + K_l\right) + \frac{1}{\rho_l}\frac{\partial}{\partial z}\left(D_{TV}\frac{\partial T^*}{\partial z} + D_{\psi V}\frac{\partial \psi}{\partial z}\right) \tag{7}$$

The liquid water flow rate u_l is described by the extended Darcy law:

Table 3. Nomenclature in Frozen Soil Parameterization (Section 2.2)

Symbol	Unit	Definition
θ_l	$m^3\,m^{-3}$	Soil volumetric liquid water content
θ_i	$m^3\,m^{-3}$	Soil volumetric ice content
ρ_l	$kg\,m^{-3}$	Intrinsic densities of liquid water, $=1000$
ρ_i	$kg\,m^{-3}$	Intrinsic densities of ice, $=920$
ρ_d	$kg\,m^{-3}$	Bulk density of a dry soil
λ_s	$W\,m^{-1}\,°C^{-1}$	Thermal conductivity of frozen soil
λ_d	$W\,m^{-1}\,°C^{-1}$	Thermal conductivity of dry soil
λ_m	$W\,m^{-1}\,°C^{-1}$	Thermal conductivity of saturated soil
λ_i	$W\,m^{-1}\,°C^{-1}$	Thermal conductivity of ice soil
k_T		A coefficient, $=0.36$
q_c		Quartz content in dry soils
w		Soil wetness
ψ	Pa	Soil matric potential
K_l	$m\,s^{-1}$	Hydraulic conductivity
D_{TV}	$kg\,m^{-1}\,s^{-1}\,°C^{-1}$	Vapor diffusive coefficient due to temperature gradient
$D_{\psi V}$	$kg\,m^{-2}\,s^{-1}$	Vapor diffusive coefficient due to matric potential gradient
T^*	$°C$	Soil temperature in the unit of $°C$
C_v	$J\,m^{-3}\,°C^{-1}$	Average volumetric heat capacity
$L_{i,l}$	$3.336 \times 10^5\,J\,kg^{-1}$	Specific latent heat of phase change (from ice to liquid water)
K_{eff}	$m\,s^{-1}$	Effective heat conductivity
u_l	$m^3\,m^{-3}$	Liquid water flow rate
c_l	$J\,K^{-1}\,g^{-1}$	Heat capacity of liquid water, $=4.195$
c_d	$J\,K^{-1}\,g^{-1}$	Heat capacity of dry soil
c_i	$J\,K^{-1}\,g^{-1}$	Heat capacity of ice, $=2.1$
g	$m\,s^{-2}$	Acceleration of gravity
Ψ_0	Pa	Saturated soil matric potential
θ_s	$m^3\,m^{-3}$	Soil porosity
B		Clapp-Hornberger constant
c_k		An adjustable constant
H	$J\,m^{-3}$	Volumetric enthalpy of water
Z	m	The vertical depth from the soil surface
m_a	kg	Total water mass

$$u_l = K_l \left[-\frac{\partial \psi}{\partial z} + 1 \right] \tag{8}$$

The freezing-point depression equation [*Li and Sun*, 2008] is as follows:

$$\Psi = \frac{L_{i,l} T^*}{g(T^* + 273.15)} \tag{9}$$

The extended empirical equation is often used for Ψ [*Koren et al.*, 1999; *Li and Sun*, 2008] as follows:

$$\Psi = \psi_0 \left(\frac{\theta_l}{\theta_s} \right)^{-b} (1 + c_k \theta_i)^2 \tag{10}$$

Combining equations (9) and (10), we obtain the following equation, which indicates the relationship between the unfrozen water content and temperature.

$$\theta_1 = \theta_s \cdot \left[\frac{L_{i,1} \cdot T^*}{g \psi_0 (T^* + 273.15)} (1 + c_k \theta_i)^{-2} \right]^{-1/b} \tag{11}$$

In the governing equations (equations (6) and (7)), which are highly nonlinear, the temperature and soil liquid moisture are taken as the prognostic variables. In addition, the term related to the ice-liquid phase change rate, $\frac{\partial \theta_i}{\partial t}$, is explicitly shown in the governing equations. Due to the large quantity of specific latent heat ($L_{i,l} = 3.336 \times 10^5$ J/kg), the term representing latent heat caused by the water-ice change, $L_{i,l} \frac{\partial \rho_i \theta_i}{\partial t}$, is closely associated with the change in soil temperature. However, the governing equations (equations (6) and (7)) must be solved through the iteration processes, and this term ($L_{i,l} \frac{\partial \rho_i \theta_i}{\partial t}$) usually generates numerical instabilities during iterations [*Hansson et al.*, 2004]. For example, let us momentarily assume that an initial condition is at a soil temperature slightly above zero without flow, and let us remove a certain amount of energy. Once freezing begins during the first numerical iteration, the soil temperature gradually decreases

while ice increases rapidly and the liquid water content simultaneously drops dramatically with little temperature change. The extra latent heat may be released in large amounts during phase transition, leading to an overestimate of the corresponding freezing of soil water and further resistance of rapid soil cooling. When this error is corrected in the second iteration, the new temperature will probably result in an estimation of low latent heat energy, thus returning the temperature to a positive value. The oscillation between these two values makes it difficult for a numerical algorithm to reach convergence at a typical time step (or at the correct temperature). Furthermore, a small error in the estimation of the phase change rate at the beginning of each iteration step will eventually introduce greater error into the temperature and volumetric moisture calculations [*Q. Li et al.*, 2009; *Bao et al.*, 2016].

To avoid instability caused by uncertainty in the estimation of the water-ice change rate, *Li and Sun* [2008] proposed a new algorithm by utilizing the two new variables: soil enthalpy $H = (C_v T^* - L_{i,l} \rho_i \theta_i)$ and total water mass $m_a = (\rho_i \theta_i + \rho_l \theta_l)$ as the predictive variables instead of the temperature and soil liquid content in the governing equations (equations (6) and (7)). The term H refers to the internal energy of the system and the potential energy for phase change, and the term m_a is employed to maintain water mass conservation in the liquid-ice phase change. Then, equations (6) and (7) can be modified into the following two equations.

$$\frac{\partial H}{\partial t} = \frac{\partial}{\partial z}\left[K_{eff}\frac{\partial T^*}{\partial z}\right] - \rho_l c_l \frac{\partial u_l T^*}{\partial z} \tag{12}$$

$$\frac{\partial m_a}{\partial t} = -\frac{\partial}{\partial z}\left(-K_l\frac{\partial\psi}{\partial z} + K_l\right) + \frac{\partial}{\partial z}\left(D_{TV}\frac{\partial T^*}{\partial z} + D_{\psi v}\frac{\partial\psi}{\partial z}\right) \tag{13}$$

Now the volumetric enthalpy H and the total water mass m_a in soil can be obtained without estimation of the water-ice phase change rate. To solve the nonlinear phase change system efficiently and stably, *Q. Li et al.* [2009] provided a detailed and explicit numerical scheme with efficient iterations to solve the full energy and water mass governing equations (H, m_a, and equation (11)) for all layers and each time step. In their numerical scheme, they designed a difference equation system by employing a linearization procedure for the nonlinear but important physical terms in equations (11)–(13). They also designed an efficient numerical iteration method to solve θ_i and T^* in the phase change. The designed numerical difference equation system from *Q. Li et al.* [2009] with efficient iterations can obtain the solution for each layer separately, step by step, and the order to obtain the solution is from the surface layer to the bottom layer. The detailed derivation and numerical scheme descriptions are presented in *Q. Li et al.* [2009].

During the iteration steps, if $T^* > 0$, the soil layer is in a thawing state, and $\theta_i = 0$, $\theta_l = m_a/\rho_l$, $T^* = H/C_v$. If $T^* < 0$, the soil layer is in a frozen state. In this case, θ_i, θ_l, and T^* should be solved iteratively by using H, m_a, and equation (11). The iteration is included in the following three steps (see Figure 3):

1. Initialize H and m_a: $H = C_v T^{*(t+1)} - L_{i,l}\rho_i\theta_i^t$, and $m_a = \rho_i\theta_i^t + \rho_l\theta_l^t$. The superscript t indicates the time step. Energy and water mass conservations are maintained by H and m_a through all iteration steps.
2. Initialize the soil state as unfrozen soil: $\theta_{i(0)} = 0$, $\theta_{l(0)} = m_a/\rho_l$, and $T^*_{(0)} = H/C_v$.
3. Solve equation (11) using the iterative method of *Q. Li et al.* [2009]. The updated ice content and soil moisture can be written as: $\theta_{i(n+1)} = (C_v T^*_{n+1} - H)/L_{i,l}\rho_i$ and $\theta_{l(n+1)} = (m_a - \rho_i\theta_{i(n+1)})/\rho_l$. The updated T^* is estimated from equation (11). The subscript n indicates the iteration step. Return to Step 3 until the increment of T^* reaches an extremely small value.

The thermal conductivity of soil is calculated by embedding the ice part of the formulas presented by *Vafai and Whitaker* [1986] into the method of *Yang et al.* [2005], who took a global soil data task formula into account.

$$\lambda_s = \lambda_d + (\lambda_m - \lambda_d)\exp\left[K_T(1 - 1/w)\right] + \lambda_i \tag{14}$$

$$\lambda_i = \theta_i K_i = \theta_i \times 2.2 \tag{15}$$

$$\lambda_d = (0.135\rho_d + 64.7)/(2700 - 0.947\rho_d) \tag{16}$$

$$\lambda_m = 0.5^{\theta_s}(7.7^{q_c}2.0^{1-q_c})^{1-\theta_s} \tag{17}$$

Similar to the above method, the volumetric heat capacity C_v is calculated as follows:

$$C_v = c_d \rho_d + c_l \rho_l \theta_l + c_i \rho_i \theta_i \qquad (18)$$

$$c_d \rho_d = (0.076 + 0.748 \rho_d / \rho_l) \times 10^6 \text{ J m}^{-3} \text{K}^{-1} \qquad (19)$$

3. Study Area and Data Set

To evaluate the newly developed LSM with coupled snow and frozen soil processes (HydroSiB2-SF), two representative stations (one snow covered and the other snow free, both with underlying frozen soil) of the Tibetan Plateau (TP) were selected for this study (see Figure 4).

The Dadongshu-Yakou station (100°14′E, 38°01′N, abbreviated as DY hereinafter) is a high-elevation snow-covered site at 4101 m in the upper Heihe River basin maintained by the Cold and Arid Region Environmental Engineering Institute, Chinese Academy of Sciences [see *X. Li et al.*, 2009]. In the winter, the largest snow
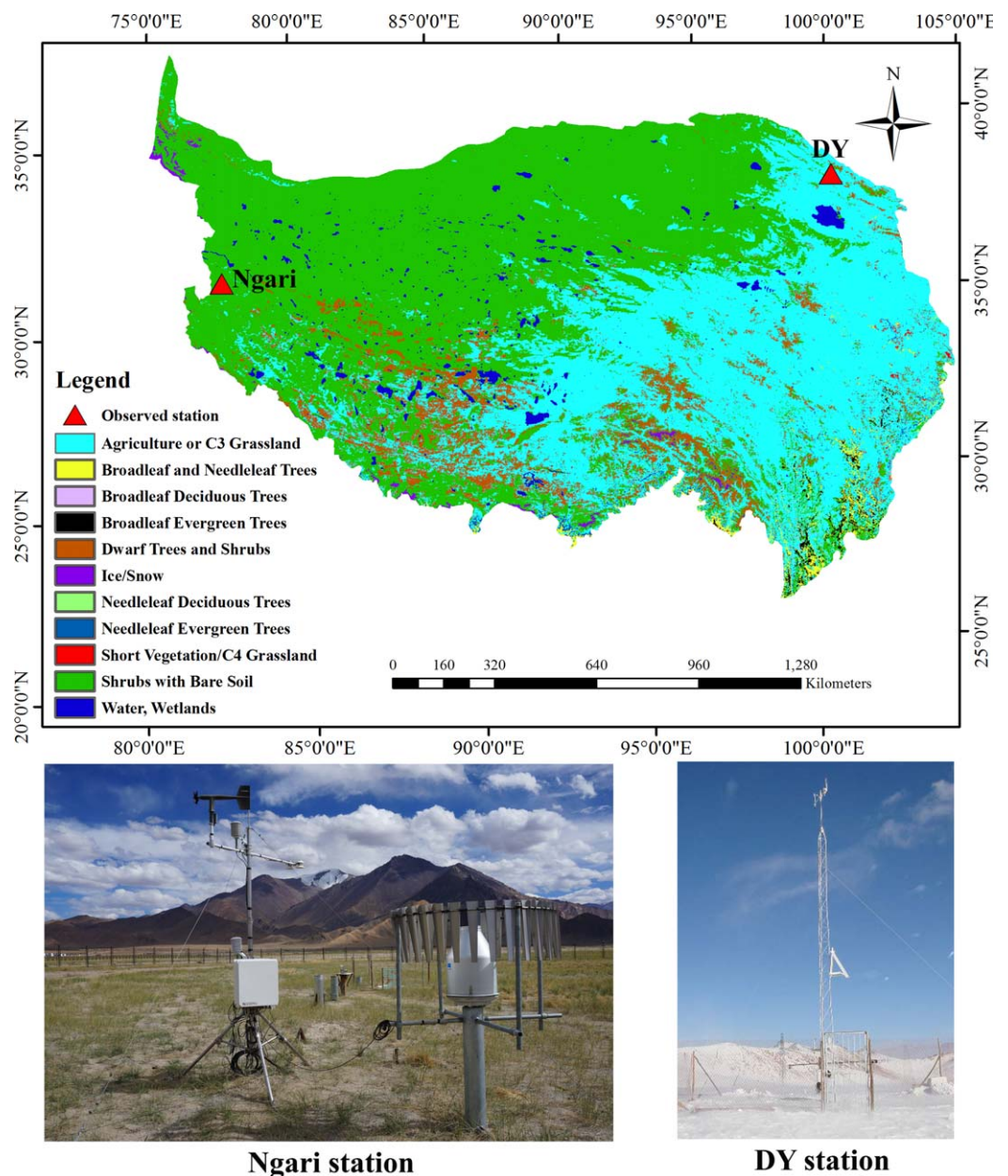

Figure 4. Location of the study sites (DY and Ngari) over the Tibetan Plateau.

depth records of DY station are approximately 0.5 m (during the study period of 2007–2008), and the average snow depth is more than 0.05 m (which is the threshold to use the three-layer snow scheme). Therefore, it is an ideal site for evaluating the coupled snow and frozen soil processes, due to its heavy snow cover during October–April and seasonal soil freezing/thawing during September–May [*Yang et al.*, 1993]. The meteorological forcing (includes hourly air temperature, wind speed, precipitation amount, downward shortwave radiation, downward longwave radiation, and relative humidity) at this station was obtained from the Watershed Allied Telemetry Experimental Research data sets [*X. Li et al.*, 2009]. In addition, the in situ measurements of snow depth, liquid soil moisture, and soil temperature for the period from 30 October 2007 to 29 October 2008 are available for model evaluation. The snow depth was measured using a snow fork, which mainly uses a CSC Sonic Ranging Sensor (requires air temperature measurement; Campbell Company, USA) within an Automatic Weather Station (AWS) at least twice a day. The near surface soil temperature (5 cm) was measured using digital thermometers, and other layers (10, 20, 40, 80, and 120 cm) were measured using soil temperature profile probes within an AWS. The liquid soil water content was determined using frequency domain portable soil moisture probes (ThetaProbe soil moisture sensor), at six depths: 5, 10, 20, 40, 80, and 120 cm every 10 min [*X. Li et al.*, 2009].

The Ngari station maintained by the Institute of Tibetan Plateau Research, Chinese Academy of Sciences, is located in a typical desert region of western TP. It has an elevation of 4256 m and was built for observing meteorology, hydrology, glaciers and lakes, atmosphere chemistry, as well as the special ecosystem over the desert environment of the western TP. The annual precipitation is very low (less than 100 mm) and highly seasonal with about 80% concentrated during May–September. The in situ observations (including the meteorological variables, soil temperature and liquid soil moisture, as well as the upward longwave and shortwave radiation) from 1 January 2011 to 31 December 2012 were used for the model inputs and evaluations in this study. The meteorological variables were observed using an AWS at the Ngari station, while soil temperature and liquid soil moisture were measured using soil temperature profile probes and soil moisture profile probes within an AWS, respectively.

The dynamic vegetation parameters include the leaf area index (LAI) and the fraction of photosynthetically active radiation (FPAR) absorbed by the green vegetation canopy; these variables can be obtained from satellite data. In this study, global LAI and FPAR MOD15_BU 1 km data sets [*Myneni et al.*, 1997] were used for both sites. These are eight-daily composites of MOD15A2 products that were obtained using the Reverb of NASA (http://reverb.echo.nasa.gov).

4. Model Evaluations

By using the in situ observations from the DY and Ngari stations, we evaluated the performance of HydroSiB2-SF by comparing the simulated results from HydroSiB2-SF, HydroSiB2-S, and HydroSiB2-F (Table 1). The bias error (BIAS) and root-mean-square error (RMSE) were adopted as evaluation criteria for the simulated results.

In the snow-covered site (DY), we focus on assessment of the improvement of snow processes by HydroSiB2-SF over HydroSiB2-F. At the snow-free site (Ngari), we concentrate on evaluating the advance of frozen soil processes by HydroSiB2-SF with respect to HydroSiB2-S. Model calibrations were performed for HydroSiB2-SF at both stations.

4.1. Evaluation at the DY Station
4.1.1. Model Calibration

The calibration for the DY station was conducted using hydraulic parameters (e.g., the soil porosity, residual soil water content, saturated hydraulic conductivity, and the two van Genuchten parameters) and thermal parameters (e.g., the saturated thermal conductivity and the dry soil thermal conductivity), which are listed in Table 4. The parameter related to the albedo of fresh snow in the visible band was also optimized.

First, the soil hydraulic parameters were calibrated based on the observed liquid soil moisture in the upper two completely thawed soil layers (5 and 10 cm depths) in July 2008 (in summer) to avoid disturbances from soil freezing/thawing (Figure 5a). Second, by keeping the calibrated soil hydraulic parameters

Table 4. The Calibrated Soil Hydraulic and Thermal Parameters for the DY Station

| Symbol	Parameters	Unit	Value
αvis0	Albedo of fresh snow in visible band		0.81
Soil Hydraulic Parameters			
θ_s	Porosity		0.64
θ_r	Residual soil water content		0.015
$K_{surface}$	Saturated hydraulic conductivity for soil surface	mm h^{-1}	2.04×10^{-5}
α	van Genuchten parameter	1 m^{-1}	0.06
n	van Genuchten parameter		1.85
anik	Anisotropy ratio for hydraulic conductivity		22.4
Soil Thermal Parameter			
Kdry	Dry soil thermal conductivity	W m^{-1} °C^{-1}	0.8
khsat	Saturated soil thermal conductivity	W m^{-1} °C^{-1}	3.6

constant, the soil thermal parameters were calibrated with respect to the observed soil temperature profile from 30 October to 31 December 2007 (in winter) (Figure 5b). Figure 5 shows that the hourly volumetric liquid soil moisture (at 5 and 10 cm depths) and the hourly soil temperature (at 5, 10, 40, and 80 cm depths) could be reasonably reproduced by HydroSiB2-SF after model calibration. The RMSEs for the liquid soil moisture were 0.041 and 0.043 m^3 m^{-3} at the 5 and 10 cm soil depths, respectively. The RMSEs for the soil temperature at the 5, 10, 40, and 80 cm depths were 2.20, 2.32, 1.62, and 2.31°C, while the BIAS values were 0.87, 1.76, 1.34, and 1.98°C, respectively. It also can be seen from Figure 5 that the simulated soil temperature at deeper soil layers (40 and 80 cm) was not reproduced as well as that in shallower soil layers (5 and 10 cm). This may be attributed to the vertical heterogeneity of the soil structure. In general, deeper soils contain more gravel (particle size $\geq$ 2 mm) in the northern Tibetan Plateau [*Pan et al.*, 2017]. Soil mixed with gravel has different thermal properties compared with fine soil (particle size < 2 mm) and thus has marked impacts on soil heat transfer [*Pan et al.*, 2017]. This will further lead to differences in soil temperature simulation at different soil depths. At present, the heterogeneity of the soil structure is not currently considered in the HydroSiB2-SF model due to a lack of corresponding in situ observations. Although there are some differences, it can be seen from Figure 5 that HydroSiB2-SF can simulate soil temperatures within a certain depth of frozen soil with acceptable accuracy.

4.1.2. Model Validation

To demonstrate the improvement of HydroSiB2-SF for the snow processes, simulations were conducted to compare HydroSiB2-SF with HydroSiB2-F at the DY station using the yearlong observations (from 30 October 2007 to 29 October 2008).

Figure 6 illustrates the improvement of snow processes by HydroSiB2-SF over HydroSiB2-F at a soil depth of 5 cm. The results show that HydroSiB2-SF accurately predicted the sharp increase in liquid soil moisture when ice melted at the beginning of May 2008, with an RMSE of 0.041 m^3 m^{-3}, while HydroSiB2-F showed a 2 month earlier ice melt, causing overestimates of liquid soil moisture in March and April 2008 (with an RMSE of 0.093 m^3 m^{-3}). The poor performance of HydroSiB2-F can be attributed to the single-layer snow scheme that does not consider the attenuation of solar radiation that penetrates into the snow pack. This deficiency has led to less energy absorbed by the snow pack but more energy been transferred into the soil layers. Consequently, HydroSiB2-F has the following characteristics: higher soil temperature, lower snow depth, more snow melt water entering into the soil, and earlier soil ice melt. Similar results were also obtained for the soil layer at the 10 cm depth (supporting information Figure S1) as well as in the deeper soil layers (not shown here).

Although the soil temperature results produced by HydroSiB2-SF are generally in good agreement with the observed values at the DY station, the simulated soil temperatures are still higher than observed values in winter (Figure 6 and supporting information Figure S1). This result may be attributed to considerable organic matter in the upper soil layers of the eastern TP. Given a large amount of organic matter in the upper soil layers, the soil will have greater porosity and thus can store more solid water (ice) in winter. This will alter the thermal properties of soil and cool the soil (leading to lower temperatures). At present, there is no detailed organic matter scheme reflected in the current version of HydroSiB2-SF because no corresponding in situ observations are available. The simulation performance should be further improved by introducing soil organic matter into soil parameterizations in future work.
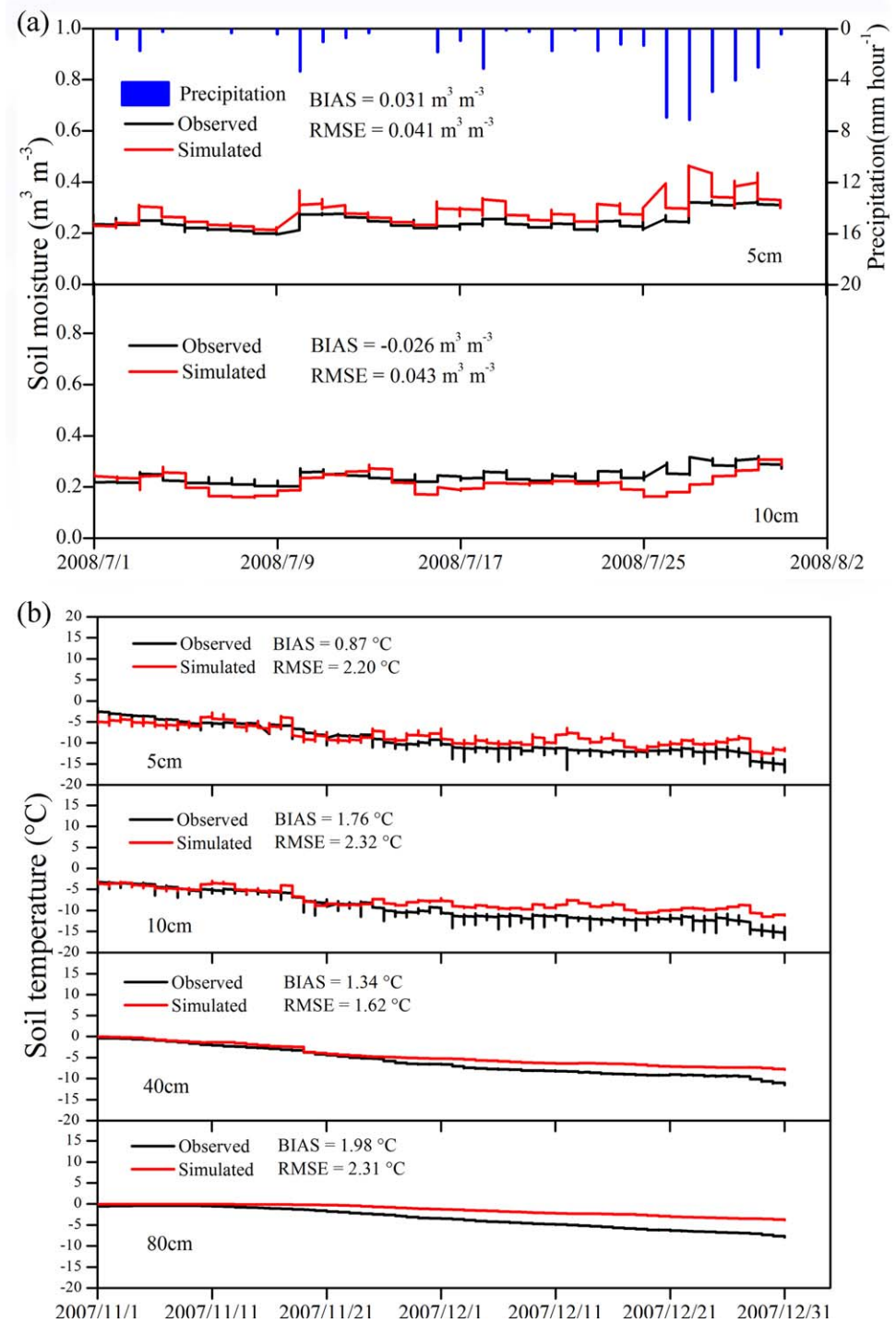
Figure 5. HydroSiB2-SF model calibration for the DY site. (a) Observed and simulated hourly volumetric liquid soil moisture at 5 and 10 cm soil depths (two upper thawed soil layers in summer) during 1–31 July 2008; (b) observed and simulated hourly soil temperature at 5, 10, 40, and 80 cm soil depths from 30 October to 31 December 2007 (in winter). The calibrated soil parameters values were also shown in Table 4.

4.2. Evaluation at the Ngari Station
4.2.1. Model Calibration
Using the same approach presented in section 4.1.1, the soil hydraulic and thermal parameters at the Ngari station were optimized and are listed in Table 5.
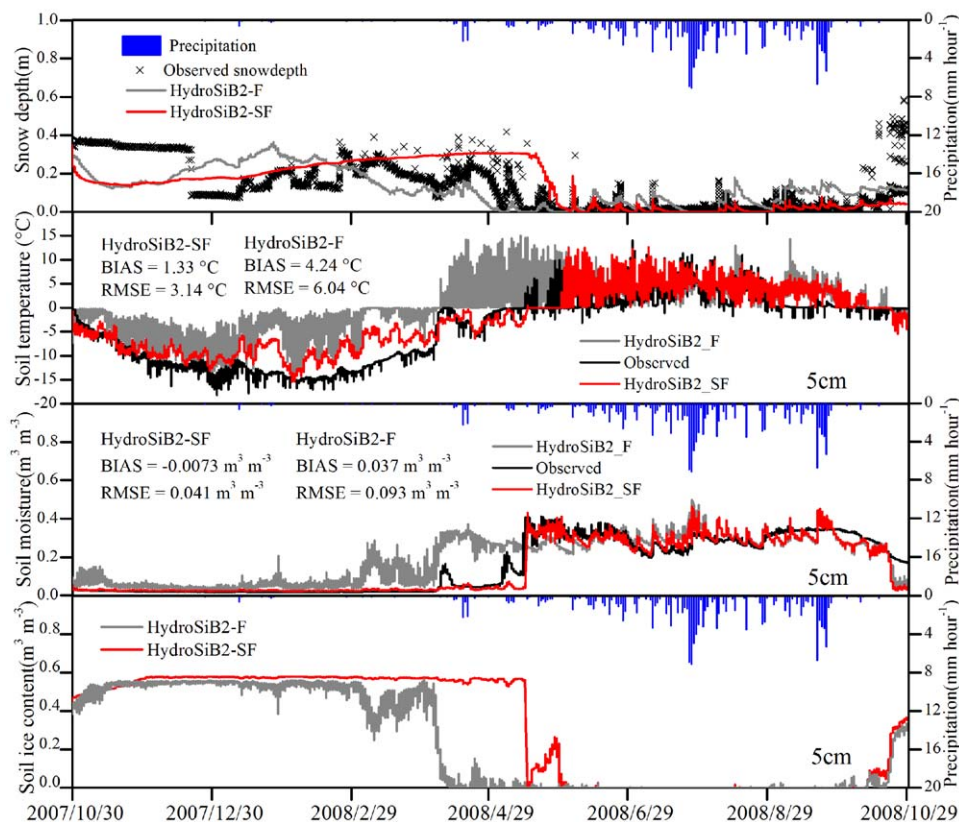
Figure 6. Comparison of the hourly simulated results (snow depth, soil temperature, volumetric liquid soil moisture, and soil ice content) at the 5 cm soil depth at the DY site between HydroSiB2-SF and HydroSiB2-F. The observed values of snow depth (black fork), soil temperature, and volumetric liquid soil moisture (black solid line) are also given.

First, the soil hydraulic parameters were calibrated with the observed liquid soil moisture at the 20 cm soil depth in a summer period (from 1 July to 31 August 2012) to avoid the disturbances from soil freezing/thawing. Second, by maintaining the calibrated soil hydraulic parameters constant, the soil thermal parameters were calibrated with the observed soil temperature at the 20 and 50 cm depths in a winter period (from 1 January to 28 February 2012). Figure 7 shows that the hourly volumetric liquid soil moisture (at the 20 cm depth) and the hourly soil temperatures (at 20 and 50 cm depths) were accurately reproduced by HydroSiB2-SF after model calibration. The RMSE and BIAS values for the liquid soil moisture were 0.0085 and 0.0056 m^3 m^{-3}, respectively. The RMSEs for the soil temperature at 20 and 50 cm were 0.83, and 0.89°C, while the corresponding BIAS values were −0.32, and 0.17°C, respectively.

4.2.2. Model Validation

To demonstrate the improvement of HydroSiB2-SF with respect to the frozen soil processes, simulations were performed to compare HydroSiB2-SF with HydroSiB2-S at the Ngari station with the 2 year observations (from 1 January 2011 to 31 December 2012).

Table 5. The Calibrated Soil Hydraulic and Thermal Parameters for the Ngari Station

Symbol	Parameters	Unit	Value
Soil Hydraulic Parameters			
θ_s	Porosity		0.4
θ_r	Residual soil water content		0.01
$K_{surface}$	Saturated hydraulic conductivity for soil surface	mm h^{-1}	1.25×10^{-5}
α	van Genuchten parameter	1 m^{-1}	0.04
n	van Genuchten parameter		1.2
anik	Anisotropy ratio for hydraulic conductivity		10
Soil Thermal Parameter			
Kdry	Dry soil thermal conductivity	W m^{-1} °C^{-1}	0.08
khsat	Saturated soil thermal conductivity	W m^{-1} °C^{-1}	0.45
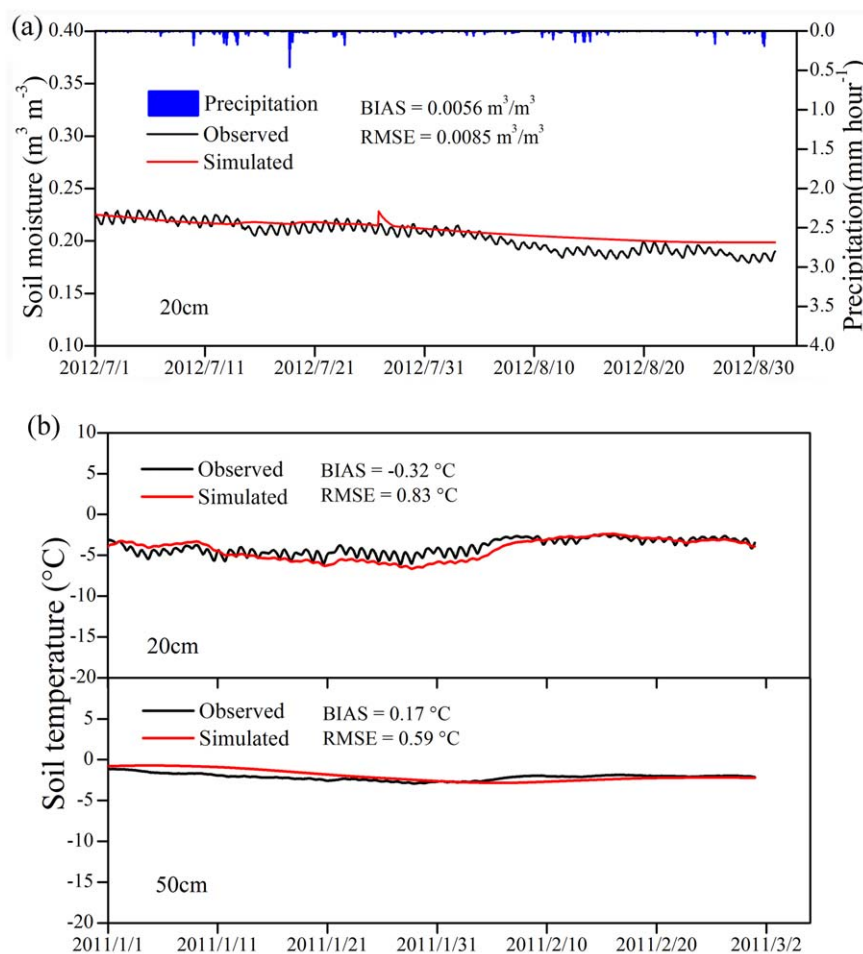
Figure 7. HydroSiB2-SF model calibration for the Ngari site. (a) Observed and simulated hourly volumetric liquid soil moisture at 20 cm depth (an upper thawed soil layer in summer) from 1 July to 31 August 2012; (b) observed and simulated hourly soil temperature at 20 and 50 cm soil depths from 1 January to 28 February 2011 (in winter). The calibrated soil parameters values were also shown in Table 5.

Figure 8 shows the superiority of HydroSiB2-SF over HydroSiB2-S for frozen soil processes at a depth of 20 cm. The results show that HydroSiB2-SF reasonably reproduced the freezing-thawing process (a decrease in liquid soil moisture during freezing and an increase in liquid soil moisture during thawing) and achieved an RMSE of 0.031 $m^3 \, m^{-3}$ and a BIAS of 0.013 $m^3 \, m^{-3}$ for the liquid soil moisture. At the beginning of the winter in 2011, the liquid soil moisture decreased rapidly by turning into ice and then began to increase during spring 2012. On the contrary, the liquid soil moisture simulated by HydroSiB2-S was relatively steady during the freezing-thawing periods, with an RMSE of 0.069 $m^3 \, m^{-3}$ and a BIAS of 0.045 $m^3 \, m^{-3}$. The results are not surprising since HydroSiB2-S cannot depict the phase change of soil water content (liquid water to/from ice) due to the absence of a frozen soil module. Furthermore, HydroSiB2-S underestimated soil temperature from November 2011 to February 2012, while HydroSiB2-SF achieved better simulation results with a BIAS of 0.66°C at the 20 cm soil depth (Figure 8). The reason for the better simulation results of HydroSiB2-SF is that when liquid soil moisture turns into ice during the soil-freezing period, the phase change of soil water releases heat that retards cooling. Similar simulation results were obtained for the soil layer at a depth of 50 cm (supporting information Figure S2).

Figure 9 shows the observed and HydroSiB2-SF-simulated frost depths from 1 August 2011 to 31 July 2012 at the Ngari station. In general, the simulated frost depths agreed well with most of the observed values (those interpolated from soil temperature profile observations), with a BIAS of −0.057 m and an RMSE of 0.13 m. The late freezing observed in the simulation may be related to the adequate snow simulation in HydroSiB2-SF, whereas Ngari station is a snow-free site.
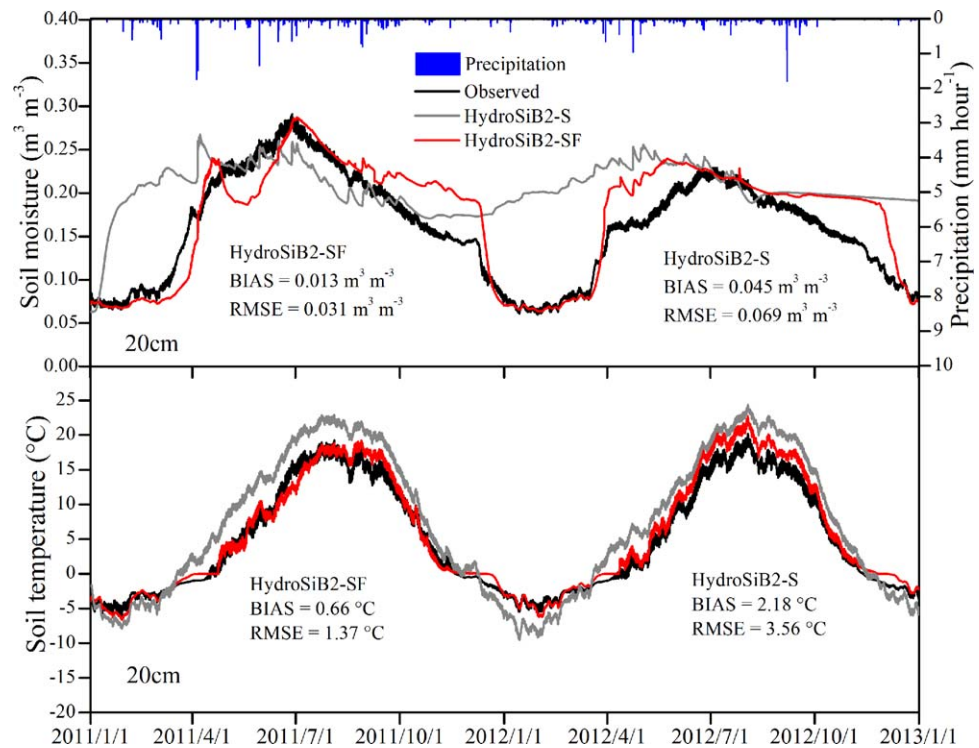
Figure 8. Comparison of the hourly observed (black solid line) and simulated volumetric liquid soil moisture and soil temperature at the 20 cm soil depth at Ngari site between HydroSiB2-SF (red line) and HydroSiB2-S (gray line).

4.3. Simulation of Upward Soil Moisture Flux During Soil Freezing at DY

Field observations have demonstrated that soil water migrates from deeper unfrozen soil layers to the frozen layer during the penetration of the freezing front [*Stähli et al.*, 1999; *Iwata and Hirota*, 2005]. However, few studies have quantitatively simulated this phenomenon using numerical models.

In this study, we studied the special soil water dynamics during soil freezing using the newly coupled model (HydroSiB2-SF). Here we used the simulations for the DY station as an example.

Figure 10 shows the simulated time-series of the volumetric soil ice content and upward soil moisture flux for the whole soil profile (10 soil layers) according to HydroSiB2-SF at the DY station. The depths of 10 soil layers are defined as 0.011, 0.016, 0.023, 0.081, 0.119, 0.139, 0.205, 0.302, 0.446, and 0.657 m. The results showed that during the freezing period (i.e., from October 2008 to February 2009), the simulated
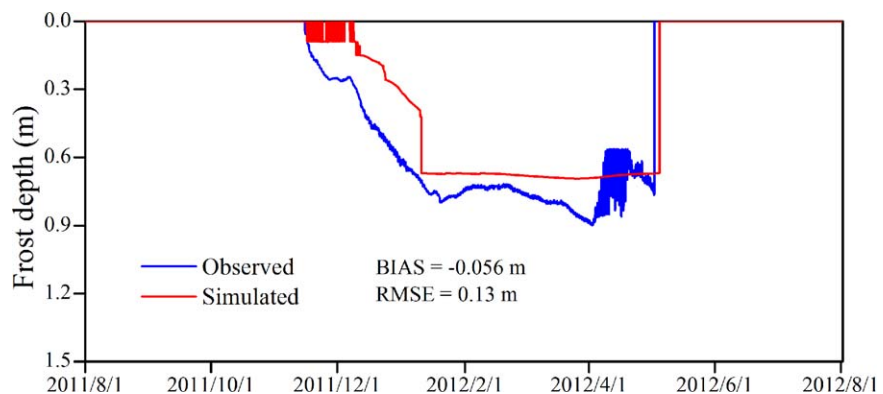
Figure 9. Hourly observed (interpolated from the observations of soil temperature profile) and simulated frost depth by HydroSiB2-SF at Ngari site from 1 August 2011 to 31 July 2012.
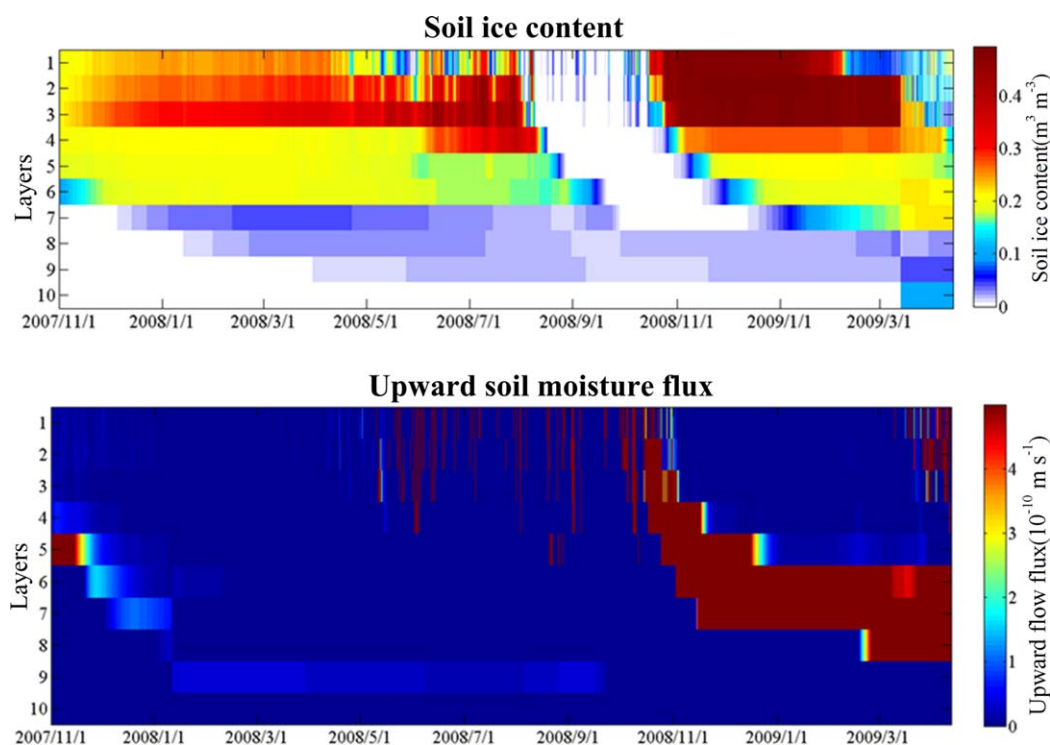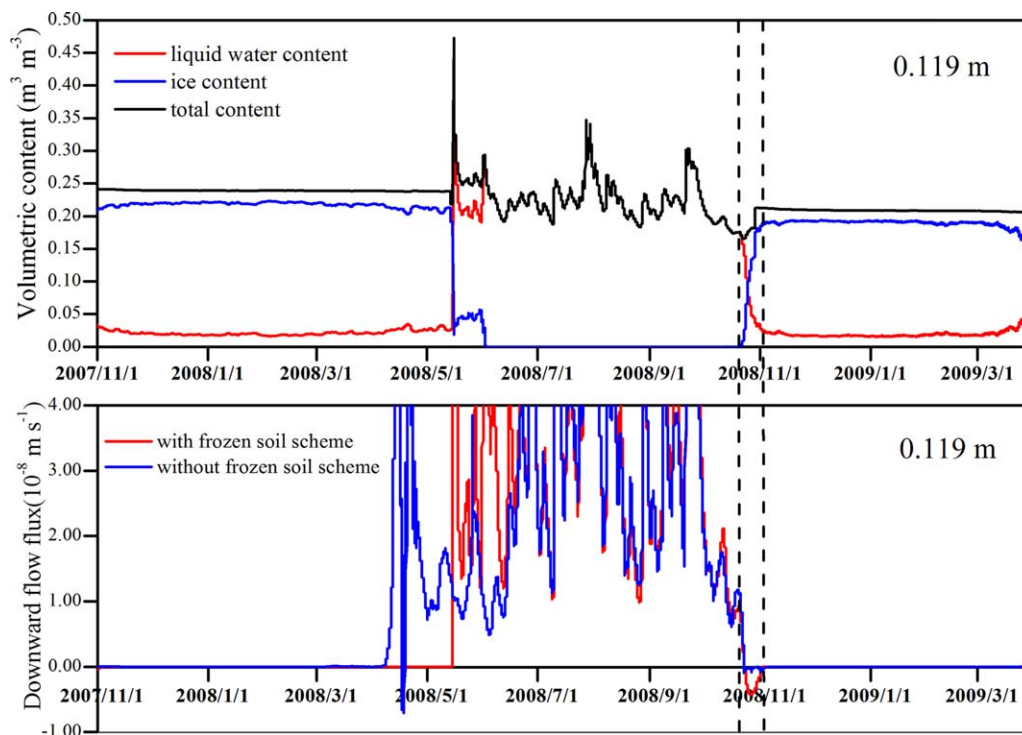
Figure 10. (top) Simulated volumetric soil ice content ($m^3\ m^{-3}$) and (bottom) upward soil moisture flux (unit: $10^{-10}\ m\ s^{-1}$) at the whole soil profile (1–10 soil layers; *y* axis) by HydroSiB2-SF at the DY site.

penetration of the freezing front (as indicated by the evolution of the soil ice content) agreed fairly well with respect to their timing and positioning with the simulated maximum of the upward soil moisture flux. This result is not surprising since the soil matric potential will sharply increase when a phase change occurs from liquid to solid water. Therefore, the progression of the freezing front largely determines the quantity of upward soil moisture flux below the frozen layer [also, see *Iwata et al.*, 2010].

Figure 11 further presents the simulated volumetric soil liquid water content, ice content, and total water content (liquid water plus ice) based on HydroSiB2-SF, as well as the downward soil moisture fluxes simulated by HydroSiB2-SF compared with HydroSiB2-S at a soil depth of 0.119 m at the DY station (the results at other depths, i.e., 0.302, 0.446, and 0.657 m, can be seen in the supporting information). It was observed that the rapid freezing periods (hereinafter RFP) clearly demonstrated the timelines for the penetration of the freezing front during 2008–2009, with a period from late-October to early November. In addition, the total simulated soil water contents increased dramatically by approximately 0.05 $m^3\ m^{-3}$ during the RFP, which can be largely attributed to the simulated (HydroSiB2-SF) upward moisture fluxes (the net water that flowed upward was approximately 1330 mm) from the underlying soils (red lines within the RFP). This occurred because the water phase changes do not add any water mass, and there is almost no precipitation-induced infiltration during winter. By contrast, HydroSiB2-S could not calculate the upward soil water transport during soil freezing that was observed in field measurements [e.g., *Stähli et al.*, 1999; *Iwata and Hirota*, 2005]. The unsuccessful result of HydroSiB2-S proved that only a model with physical parameterizations of both the processes of soil freezing/thawing and interlayer moisture exchanges in unsaturated soil can capture the special upward moisture movement caused by the sudden increase in soil matric potential during rapid soil freezing.

From Figure 11, we also observed that in spring (late April and May 2008 in this study), HydroSiB2-S (without the frozen soil scheme) showed obvious infiltration (downward water fluxes) in the upper soil layers (0.119 m) because the presence of ice was neglected. However, HydroSiB2-SF, which accounts for the existence of ice (solid water), largely blocked the downward infiltration into deeper soils in spring (see red lines in the bottom of the subfigures). To reasonably simulate/predict reduced infiltration is important because the associated increased runoff will exacerbate the spring floods induced by snowmelt. After rapid ice melt,

Figure 11. Simulated volumetric soil liquid water content, ice content, and total water content (unit: m³/m³) by HydroSiB2-SF (top in each subfigure); as well as the simulated downward soil moisture fluxes (unit: m/s; where the upward fluxes have negative values; bottom in each subfigure) by HydroSiB2-SF (with frozen soil scheme) comparing to HydroSiB2-S (without frozen soil scheme) at the depth of 0.119 m at DY site, where the rapid freezing periods (RFP) are indicated by two dashed parallel lines.

HydroSiB2-SF tended to generate a liquid soil water content and downward water fluxes similar to HydroSiB2-S during summer.

5. Conclusions

In this study, an LSM with coupled snow and frozen soil physics was developed by improving the formulations of snow and frozen soil for a hydrologically improved LSM (HydroSiB2). First, an energy-balance-based three-layer snow model was incorporated into HydroSiB2 (hereafter HydroSiB2-S) for an improved description of internal processes of the snow pack. Second, a universal and simplified soil model was coupled with HydroSiB2-S to account for soil water freezing and thawing (hereafter HydroSiB2-SF). In order to avoid the instability caused by estimating water phase changes, enthalpy was adopted as a prognostic variable instead of snow/soil temperature in the energy balance equation of the snow/frozen soil module.

For an improved understanding of the snow and frozen soil processes, the newly developed cryosphere LSM (HydroSiB2-SF) as well as its two variants (HydroSiB2-F and HydroSiB2-S; see Table 1 for model descriptions) were then carefully evaluated and compared for two sites of the Tibetan Plateau (TP). Through a comparison of HydroSiB2-SF and HydroSiB2-F for a snow-covered site, we clearly demonstrated the importance of representing internal snowpack processes using a multilayer structure that calculates the absorption of incident solar radiation. Similarly, through a comparison of HydroSiB2-SF and HydroSiB2-S for a snow-free site, we clearly showed the importance of formulating the soil freezing/thawing processes in cryosphere land surface modeling. Although an internal iterative method is embedded in the frozen soil module, the module can also simulate freezing and thawing processes over a short time scale with a low computation cost. At the DY site, one run of HydroSiB2-SF cost 5 s on a PC (CPU: 3.6 GHz, 64 bit operating system) at a 1 h time step for a 1 year simulation, while HydroSiB2-F cost 4 s on a PC for the same simulation. At the Ngari site, one run of HydroSiB2-SF cost 10 s on a PC at a 1 h time step for the 2 year simulation, while HydroSiB2-S cost 8 s for the same simulation. Therefore, the time required for the HydroSiB2-SF and HydroSiB2-S (or HydroSiB2-F) calculations is almost the same and is not high.

Through simultaneous calculation of a temporally variable volumetric soil ice content (that indicates a progression of the freezing front) and soil moisture fluxes in the soil profile (1–10 soil layers) of a snow-covered site of the TP, the new model (HydroSiB2-SF) has demonstrated the capability of simulating the special upward water movement toward the freezing front from the underlying soil layers during winter. Therefore, HydroSiB2-SF can be a realistic modeling tool for studying cold region soil water dynamics, and thereby contribute to an improved understanding of the cryosphere hydrological processes.

Finally, it is expected that in the near future, the new LSM could be coupled with an atmospheric general circulation model or a regional climate model for an improved simulation of land surface fluxes and thereby yield refined predictions of future climate for the Tibetan Plateau and its surroundings. On the other hand, since this model has the limitation that flow and transport are restricted to the vertical dimension, it should be further coupled with a distributed hydrological model for basin-wide hydrological studies (e.g., to explore the influence of cryosphere changes on river runoff).

References

Bao, H., T. Koike, K. Yang, L. Wang, M. Shrestha, and P. Lawford (2016), Development of an enthalpy-based frozen soil model and its validation in a cold region in China, *J. Geophys. Res. Atmos.*, *121*, 5259–5280, doi:10.1002/2015JD024451.

Cherkauer, K. A., L. C. Bowling, and D. P. Lettenmaier (2003), Variable infiltration capacity cold land process model updates, *Global Planet. Change*, *38*, 151–159.

Dall'Amico, M., S. Endrizzi, S. Gruber, and R. Rigon (2011), A robust and energy-conserving model of freezing variably-saturated soil, *Cryosphere*, *5*, 469–484, doi:10.5194/tc-5-469-2011.

Dickinson, R. E., A. Henderson-Sellers, and P. J. Kennedy (1993), Biosphere-Atmosphere Transfer Scheme (BATS) Version 1e as coupled to the NCAR Community Climate Model, *NCAR Tech. Note TN–387 1 STR*, 72 pp., Boulder, Colo.

Ding, B., K. Yang, J. Qin, L. Wang, Y. Chen, and X. He (2014), The dependence of precipitation types on surface elevation and meteorological conditions and its parameterization, *J. Hydrol.*, *513*, 154–163.

Essery, R., E. Martin, H. Douville, A. Fernández, and E. Brun (1999), A comparison of four snow models using observations from an alpine site, *Clim. Dyn.*, *15*, 583–593.

Essery, R., D. Marks, and P. Marsh (2009), Subsurface, surface and atmospheric processes in cold regions hydrology, *Hydrol. Processes*, *23*, 2496–2497.

Flerchinger, G. N., and K. E. Saxton (1989), Simultaneous heat and water model of freezing snow-soil system. Field verification, *Trans. ASAE*, *32*, 573–578.

Gusev, Y. M., and O. N. Nasonova (1998), The land surface parameterization scheme SWAP: Description and partial validation, *Global Planet. Change*, *19*, 63–86.

Hansson, K., J. Simunek, M. Mizoguchi, L. Lundin, and M. van Genuchten (2004), Water flow and heat transport in frozen soil: Numerical solution and freeze-thaw applications, *Vadose Zone J.*, *3*(2), 693–704.

Iwata, Y., and T. Hirota (2005), Monitoring over-winter soil water dynamics in a freezing and snow-covered environment using a thermally insulated tensiometer, *Hydrol. Processes*, *19*, 3013–3019, doi:10.1002/hyp.5813.

Iwata, Y., T. Hirota, M. Hayashi, S. Suzuki, and S. Hasegawa (2010), Effects of frozen soil and snow cover on cold-season soil water dynamics in Tokachi, Japan, *Hydrol. Processes*, *24*(13), 1755–1765.

Jansson, P. E., and D. S. Moon (2001), A coupled model of water, heat and mass transfer using object orientation to improve flexibility and functionality, *Environ. Modell. Software*, *16*, 37–46.

Jaranilla-Sanchez, P. A., L. Wang, and T. Koike (2011), Modeling the hydrologic responses of the Pampangga River Basin in the Philippines: A quantitative approach for identifying droughts, *Water Resour. Res.*, *47*, W03514, doi:10.1029/2010WR009702.

Koren, V., J. Schaake, K. Mitchell, Q.-Y. Duan, F. Chen, and J. M. Baker (1999), A parameterization of snowpack and frozen ground intended for NCEP weather and climate models, *J. Geophys. Res.*, *104*(D16), 19,569–19,585.

Kurylyk, B. L., K. T. B. MacQuarrie, and J. M. McKenzie (2014), Climate change impacts on groundwater and soil temperatures in cold and temperate regions: Implications, mathematical theory, and emerging simulation tools, *Earth Sci. Rev.*, *138*, 313–334.

Lebedeva, L., O. Semenova, and T. Vinogradova (2014), Simulation of active layer dynamics, Upper Kolyma, Russia, using the hydrograph hydrological model, *Permafrost Periglac. Process.*, *25*, 270–280.

Li, Q., and S. Sun (2008), Development of the universal and simplified soil model coupling heat and water transport, *Sci. China Ser. D: Earth Sci.*, *51*(1), 88–102.

Li, Q., S. Sun, and Q. Dai (2009), The numerical scheme development of a simplified frozen soil model, *Adv. Atmos. Sci.*, *26*(5), 940–950, doi:10.1007/s00376-009-7174-z.

Li, X., G. Cheng, H. Jin, E. Kang, T. Che, R. Jin, L. Wu, Z. Nan, J. Wang, and Y. Shen (2008), Cryospheric change in China, *Global Planet. Change*, *62*, 210–218.

Li, X., et al. (2009), Watershed allied telemetry experimental research, *J. Geophys. Res.*, *114*, D22103, doi:10.1029/2008JD011590.

Myneni, R. B., R. R. Nemani, and S. W. Running (1997), Algorithm for the estimation of global land cover, LAI and FPAR based on radiative transfer models, *IEEE Trans. Geosci. Remote*, *35*, 1380–1393.

Niu, G.-Y., and Z.-L. Yang (2006), Effects of frozen soil on snowmelt runoff and soil water storage at a continental scale, *J. Hydometeorol.*, *7*, 937–952.

Niu, G.-Y., et al. (2011), The community Noah land surface model with multiparameterization options (Noah-MP): 1. Model description and evaluation with local-scale measurements, *J. Geophys. Res.*, *116*, D12109, doi:10.1029/2010JD015139.

Pan, Y., S. Lyu, S. Li, Y. Gao, X. Meng, Y. Ao, and S. Wang (2017), Simulating the role of gravel in freeze–thaw process on the Qinghai–Tibet Plateau, *Theor. Appl. Climatol.*, *127*, 1011–1022.

Pauwels, V. R. N., and E. F. Wood (1999), A soil-vegetation-atmosphere transfer scheme for the modeling of water and energy balance processes in high latitudes: 1. Model improvements, *J. Geophys. Res.*, *104*(D22), 27,811–27,822.

Qi, W., C. Zhang, G. Fu, and H. Zhou (2015), Global land data assimilation system data assessment using a distributed biosphere hydrological model, *J. Hydrol.*, *528*, 652–667.

Sellers, P. J., D. A. Randall, G. J. Collatz, J. A. Berry, C. B. Field, D. A. Dazlich, C. Zhang, G. D. Collelo, and L. Bounoua (1996), A revised land surface parameterization (SiB2) for atmospheric GCMs, part I: Model formulation, *J. Clim.*, *9*, 676–705.

Shrestha, M., L. Wang, T. Koike, Y. Xue, and Y. Hirabayashi (2010), Improving the snow physics of WEB-DHM and its point evaluation at the SnowMIP sites, *Hydrol. Earth Syst. Sci.*, *14*, 2577–2594.

Shrestha, M., L. Wang, T. Koike, Y. Xue, and Y. Hirabayashi (2012), Modeling the spatial distribution of snow cover in the Dudhkoshi Region of the Nepal Himalayas, *J. Hydrometeorol.*, *13*, 204–222.

Shrestha, M., L. Wang, T. Koike, H. Tsutsui, Y. Xue, and Y. Hirabayashi (2014), Correcting basin-scale snowfall in a mountainous basin using a distributed snowmelt model and remote sensing data, *Hydrol. Earth Syst. Sci.*, *18*, 747–761.

Smirnova, T. G., J. M. Brown, S. G. Benjamin, and D. Kim (2000), Parameterization of cold-season processes in the MAPS land-surface scheme, *J. Geophys. Res.*, *105*(D3), 4077–4086.

Stähli, M., P. E. Jansson, and L. C. Lundin (1999), Soil moisture redistribution and infiltration in frozen sandy soils, *Water Resour. Res.*, *35*(1), 95–103, doi:10.1029/1998WR900045.

Sun, S., and Y. Xue (2001), Implementing a new snow scheme in Simplified Simple Biosphere Model (SSiB), *Adv. Atmos. Sci.*, *18*, 335–354.

Sun, S. F., J. M. Jin, and Y. Xue (1999), A simple snow-atmosphere-soil transfer model, *J. Geophys. Res.*, *104*(D16), 19,587–19,597.

Vafai, K., and S. Whitaker (1986), Simultaneous heat and mass transfer accompanied by phase change in porous insulation, *J. Heat Transfer*, *108*(1), 132–140.

Van Genuchten, M. T. (1980), A closed form equation for predicting the hydraulic conductivity of unsaturated soils, *Soil Sci. Soc. Am. J.*, *44*, 892–898.

Wang, F., L. Wang, H. Zhou, O. Saavedra, T. Koike, and W. Li (2012), Ensemble hydrological prediction based real-time optimization of multi-objective reservoir during flood season in a semiarid basin with global numerical weather predictions, *Water Resour. Res.*, *48*, W07520, doi:10.1029/2011WR011366.

Wang, L., T. Koike, D. Yang, and K. Yang (2009a), Improving the hydrology of the Simple Biosphere Model 2 and its evaluation within the framework of a distributed hydrological model, *Hydrol. Sci. J.*, *54*(6), 989–1006, doi:10.1623/hysj.54.6.989.

Wang, L., T. Koike, K. Yang, T. Jackson, R. Bindlish, and D. Yang (2009b), Development of a distributed biosphere hydrological model and its evaluation with the Southern Great Plains Experiments (SGP97 and SGP99), *J. Geophys. Res.*, *114*, D08107, doi:10.1029/2008JD010800.

Wang, L., T. Koike, K. Yang, and P. Yeh (2009c), Assessment of a distributed biosphere hydrological model against streamflow and MODIS land surface temperature in the upper Tone River Basin, *J. Hydrol.*, *377*, 21–34.

Warrach, K., H. Mengelkamp, and E. Raschke (2001), Treatment of frozen soil and snow cover in the land surface model SEWAB, *Theor. Appl. Climatol.*, *69*, 23–37.

Woo, M. K (2012), *Permafrost Hydrology*, Springer Sci. and Bus. Media., Springer-Verlag Berlin Heidelberg.

Xiao, Y., L. Zhao, Y. Dai, R. Li, Q. Pang, and J. Yao (2013), Representing permafrost properties in CoLM for the Qinghai-Xizang (Tibetan) Plateau, *Cold Reg. Sci. Technol.*, *87*, 68–77.

Xue, Y., P. J. Sellers, J. L. Kinter, and J. Shukla (1991), A simplified biosphere model for global climate studies, *J. Clim.*, *4*, 345–364.

Xue, Y., S. Sun, D. S. Kahan, and Y. Jiao (2003), Impact of parameterizations in snow physics and interface processes on the simulation of snow cover and runoff at several cold region sites, *J. Geophy. Res.*, *108*(D22), 8859, doi:10.1029/2002JD003174.

Yang, K., T. Koike, B. Ye, and L. Bastidas (2005), Inverse analysis of the role of soil vertical heterogeneity in controlling surface soil state and energy partition, *J. Geophys. Res.*, *110*, D08101, doi:10.1029/2004JD005500.

Yang, Z.-L., R. E. Dickinson, A. Robock, and K. Y. Vinnikov (1997), Validation of the snow submodel of the Biosphere-Atmosphere Transfer Scheme with Russian snow cover and meteorological observational data, *J. Clim.*, *10*, 353–373.

Yang, Z.-N., Z. Yang, F. Liang, and Q. Wang (1993), Permafrost hydrological processes in Binggou Basin of Qilian Mountains [in Chinese with English abstract], *J. Glaciol. Geocryol.*, *15*(2), 235–241.

Zhang, T. (2005), Influence of the seasonal snow cover on the ground thermal regime: An overview, *Rev. Geophys.*, *43*, RG4002, doi:10.1029/2004RG000157.

Zhang, T., R. G. Barry, K. Knowles, J. A. Heginbottom, and J. Brown (1999), Statistics and characteristics of permafrost and ground-ice distribution in the Northern Hemisphere, *Polar Geogr.*, *23*, 132–154, doi:10.1080/10889379909377670.

Zhao, L., D. M. Gray, and D. H. Male (1997), Numerical analysis of simultaneous heat and mass transfer during infiltration into frozen ground, *J. Hydrol.*, *200*, 345–363.

Zhou, J., L. Wang, Y. Zhang, Y. Guo, X. Li, and W. Liu (2015), Exploring the water storage changes in the largest lake (Selin Co) over the Tibetan Plateau during 2003–2012 from a basin-wide hydrological modeling, *Water Resour. Res.*, *51*, 8060–8086, doi:10.1002/2014WR015846.